J. Fluid Mech. (2011), *vol.* 671, *pp.* 384–398. © Cambridge University Press 2011
doi:10.1017/S0022112010005756

Highly transient squeeze-film flows

E. A. MOSS†, A. KRASSNOKUTSKI,
B. W. SKEWS AND R. T. PATON

School of Mechanical Engineering, University of the Witwatersrand, Private Bag 3,
WITS 2050, South Africa

(Received 9 February 2010; revised 1 November 2010; accepted 2 November 2010;
first published online 25 January 2011)

The aim of this work was to investigate the flow evolution with time of fluid between two parallel disks and the corresponding pressure variations at the centre of the lower disk that occur subsequent to an impact-loading situation arising from dropping a mass onto the upper disk from a chosen height. During the event a fixed amount of energy is dissipated in the fluid between the disks through the action of friction. Therefore, this fundamental system may be regarded as a constant energy one, as distinct from one in which the upper disk is moving at a constant velocity, or is acted upon by a constant force. A test cell was set up to conduct the investigation, for which the separation between the disks was monitored, together with the pressure at the centre of the lower disk, over the duration of the experiment (about 8–10 ms). Glycerine was used as the test fluid. The equation of motion, based on a self-similarity approach, was reduced to a simpler (quasi-steady linear or QSL) form. Measured values of disk separation, velocity and acceleration were substituted as inputs into the full QSL model and two limiting cases, namely an inviscid and a viscous model. The QSL model provided excellent comparisons between the pressure measurements and data generated by a commercial computational fluid dynamics software package, throughout the duration of a typical experiment. The inviscid and viscous models achieved good correlations with measurements for the initial impact (during which disk accelerations exceeding $2\,\mathrm{km\,s^{-2}}$ occurred) and towards the end of the event, that were characterized by a small and much larger pressure rise, respectively. The former feature appears not to have been previously reported and is likely to typify that which would be observed in impact systems involving squeeze films.

Key words: general fluid mechanics, lubrication theory, Navier–Stokes equations

1. Introduction

Squeeze-film systems have important practical applications (e.g. lubrication systems, shock absorbers and human joints). Here we examine Newtonian squeeze flow between parallel disks, arising from rapid motion caused by an impact. A comprehensive review of squeeze flows has been given by Engmann, Servais & Burbidge (2005), and therefore we restrict our discussion mainly to previous work concerning the effects of inertia.

The first broadly relevant papers are those of Stefan (1874) and Reynolds (1886), who considered Newtonian flows for physical situations in which fluid inertia effects are small – and for which simple analytical solutions exist. The earliest work that takes proper cognizance of inertia effects is that of Ishizawa (1966), who assumed

† Email address for correspondence: edward.moss@wits.ac.za

https://doi.org/10.1017/S0022112010005756 Published online by Cambridge University Press

that the radial velocity profiles ($v_r(r, z, t)$, where r, z and t are the radial and axial coordinates and time respectively) were radially self-similar in shape at any instant of time and scaled in magnitude according to $-[r/(2h)]\mathrm{d}h/\mathrm{d}t$ (h is the disk separation). (This is frequently referred to as the parallel assumption in the literature, in which material planes that are initially radial remain so during the subsequent deformation.) According to flow continuity, Ishizawa obtained transverse velocities $v_z(z)$ that are independent of radius, leading to a partial differential equation with two independent variables ($\eta \equiv z/h$ and t) rather than three (r, z and t). He solved the simplified equation through a perturbation technique in which time variations were embedded in the perturbation parameter, noting that the solutions were in principle limited to Reynolds number Re values less than unity ($Re \equiv h\dot{h}/\nu$, where $\dot{h}$ and ν are the disk relative approach velocity and kinematic viscosity respectively). He also showed that the special (and limiting) case given by a disk separation variation of the form $\sqrt{1-\alpha t}$ reduces the problem to the solution of an ordinary differential equation, an approach that was subsequently adopted by Wang (1976) (also in the context of a perturbation approach) and much more recently by Rashidi, Shahmohamadi & Dinarvand (2008) who used a homotopy analysis for the solution of the same equations.

Ishizawa was followed by Kuzma (1967) who used the first term of a successive approximation approach (in effect a truncated perturbation method) to obtain successful correlations with measurements of disk separation in a situation in which the load was assumed to be constant, with values of the Reynolds number up to at least 60. In this instance, mercury was used as the working fluid (for its low value of the kinematic viscosity), and inertia effects were demonstrably present – i.e. there were significant differences between predictions including and excluding inertia effects respectively. Authors such as Jones & Wilson (1975) and Tichy & Modest (1978) also took cognizance of inertia effects for Newtonian flows, by making use of the parallel assumption in a fashion equivalent to that of Ishizawa (1966) and solving the resultant equations through perturbation methods. Tichy (1981) noted that most of the perturbation solutions, while strictly valid only for $Re < 1$, surprisingly gave accurate results for Reynolds numbers typically up to the range 7–10 (and apparently up to 60 in the case of Kuzma). Tichy's alternative approach was to linearize the Navier–Stokes equations in a way similar to Oseen (1927), leading to an approximate solution that is valid up to high Reynolds numbers.

The self-similarity approach adopted by Ishizawa (1966) and others should be seen in the context of the so-called infinite energy solutions, also known as the Berman solutions after Berman (1953), that are typically characterized by unbounded domains. In investigating the stability of two-dimensional squeeze flows that vary slowly with time and space, Stuart *et al.* (1990) adopted a similarity formulation, based on a large ratio of plate separation to plate breadth. Most studies (e.g. Brady & Acrivos 1981; Brady 1984; Espin & Papageorgiou 2009) have established the validity limits of self-similarity solutions by comparing them with numerical computations based on the full Navier–Stokes equations. Espin & Papageorgiou (2009), in a study of accelerating and decelerating channel flows in finite domains, noted that self-similar flows do not arise in truncated domains 'unless the Reynolds number is sufficiently small and/or appropriate conditions are imposed at the inlet'. Their numerical investigation showed that self-similarity solutions can occur for Reynolds numbers less than approximately 500 and 33 for accelerating and decelerating flows respectively. Despite the body of literature related to evaluating the limitations of self-similarity approaches for various flow systems, axisymmetric squeeze films appear not to have been subjected

https://doi.org/10.1017/S0022112010005756 Published online by Cambridge University Press

to a comprehensive evaluation. However, Drazin & Riley (2006) have noted that the self-similar assumptions apply to squeeze films everywhere, except within a distance $O(h_0)$ from the edge. Thus, the accuracy of the self-similarity solutions in confined domains of this type improves as $h_0/R \to 0$ (where h_0 is the initial disk separation and R is the disk radius), and hence these exact solutions are most likely to be seen near the axis of symmetry.

Hamza & MacDonald (1981) concentrated on the physical situation in which one disk was stationary and the other accelerated rapidly (over a short but non-zero time) from rest to a state of constant velocity, covering the Reynolds number range (based on the initial disk separation and the final disk velocity) $96 \geqslant Re \geqslant 0.5$ and distinguishing between the large inertia at start-up and the later phase in which friction forces dominate. Values of $(1/r)\partial p/\partial r$ were computed (and in part supported by linear theory), encapsulating the vorticity diffusion that occurs away from both of the disks as the moving disk approaches the stationary one.

Weinbaum, Lawrence & Kuang (1985) studied the draining of a fluid layer between two axisymmetric disks under a constant normal force applied to a mass that is in contact with the upper disk. They formulated the problem assuming self-similar velocity profiles in the gap, while taking cognizance of inertia effects of the fluid and of the moving body. In so doing they identified two important dimensionless groups: the Reynolds number (Re) based on the initial disk separation and a characteristic inertial settling velocity and a further group (β) that is the ratio of the squares of the gravitational and fluid inertia settling times. They solved the equations in the infinite-Re limit for $\beta \to 0$ (hydrodynamic pressure instantaneously supports its weight) and $\beta \to \infty$ (the top disk falls virtually as though in a vacuum) and at early times (when $h \sim h_0$) for all values of β. In addition they obtained solutions for small β in the limiting cases $Re \ll 1$, $h \sim h_0$ and $Re \gg 1$. Lawrence, Kuang & Weinbaum (1985) considered the same case as Weinbaum *et al.* (1985) (i.e. draining between disks under a constant normal force) but ignored the inertia of the moving body. They developed an approximate large-Re solution, using an integral approach that compared favourably with numerical predictions.

Relatively few comprehensive experimental investigations exist for Newtonian flows. The equation of Stefan (1874) has been well verified in the literature – for example by Brindley, Davies & Walters (1976) who computed variations of h for fixed applied loads and Phan-Thien *et al.* (1985) who obtained time variations of load for fixed values of $\dot{h}$. However, studies including inertia effects have been relatively neglected. Exceptions are (i) the experiments of Kuzma, Maki & Donnelly (1964) that covered Re values up to about 60 for a constant applied force and (ii) the case of an upper surface rapidly accelerated to a fixed velocity, which gave good correlations (force variations with time) with regular perturbation theory up to an Re of at least 14 (Tichy & Winer 1970).

This research has been motivated by two basic issues. Firstly, while the constant velocity and constant force cases have been well exploited in the literature, the pressures generated have been small in all instances, and none of the previous studies expressly considered the equally fundamental case of requiring a given amount of kinetic energy of a falling mass to be dissipated over a small distance through the generation of fluid forces between two disks.

This may be achieved by conducting an experiment in which a mass is dropped from a given height onto a top disk that is initially at rest and separated from a stationary lower disk by a defined fluid interface thickness. While some of the potential energy is lost during the descent of the weight, a further quantum is dissipated during

https://doi.org/10.1017/S0022112010005756 Published online by Cambridge University Press

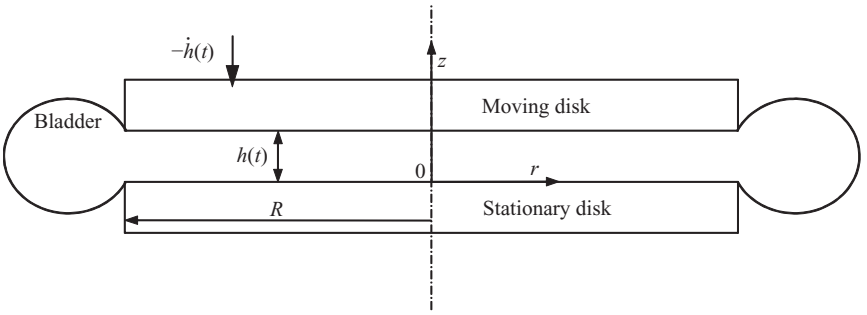


FIGURE 1. Geometry of parallel-disk arrangement.

the weight/disk contact, and some fluid escapes from the outer radii of the disks, carrying kinetic energy with it; the largest proportion of energy is dissipated within the fluid volume. We refer to this subsequently as the constant energy case, with the transmission efficiency defined as the ratio of the energy dissipated in the fluid to the original gravitational potential energy of the weight from its released height. Because experiments in which the initial fluid volume between the disks is small may be conducted, the average pressures so generated can be easily made high.

Secondly, an elementary analysis shows that the ratio of temporal to spatial inertia in the Navier–Stokes equations is $O(\ddot{h}h/\dot{h}^2 - 2)$, and it is appropriate to define this dimensionless grouping as a parameter $\Re$. While it is tacit that the theoretical study of Hamza & MacDonald (1981) would have embraced large values of $\Re$ during the initial stages of motion, if (for example) the experimental data of Kuzma *et al.* (1964) are roughly analysed in this light, their $\Re$ is $O(1)$. We therefore consider it fundamentally interesting to examine a dynamic situation in which $\Re \gg 1$.

Arising from the foregoing, the aim of this investigation was to use transient pressure and displacement measurements, together with theoretical considerations, to explore the nature of the highly transient Newtonian flow system that evolves between two initially separated axisymmetric disks under the rapid-loading conditions induced by the impact of a falling mass. This system, distinct from those that have been studied previously (constant velocity or force), comprises one in which a constant amount of *energy* is dissipated by the time-dependent radial flow between parallel disks.

2. Experimentation

The system under consideration is shown in figure 1. Two parallel, circular disks of radius R are separated at any time by a distance h and have an incompressible Newtonian liquid between them. A thin bladder made of light rubber is incorporated into the experimental system to contain the liquid and is also shown here for clarity. The z-coordinate system is defined in the upward direction relative to the stationary lower disk, while the upper one has a motion in the negative z-direction of magnitude $\dot{h}$.

Impact was achieved using a drop-weight tester (not shown), in which masses may be dropped from variable heights between two guide rails. Experiments were conducted using a test cell bolted firmly onto the base of the test rig and comprising two parallel disks of diameter 120 mm with a simple bladder of cross-sectional diameter 50 mm to contain the fluid in a controlled way (figure 2*a*,*b*). The plates were designed and manufactured in such a way that their distortion was minimal during

https://doi.org/10.1017/S0022112010005756 Published online by Cambridge University Press

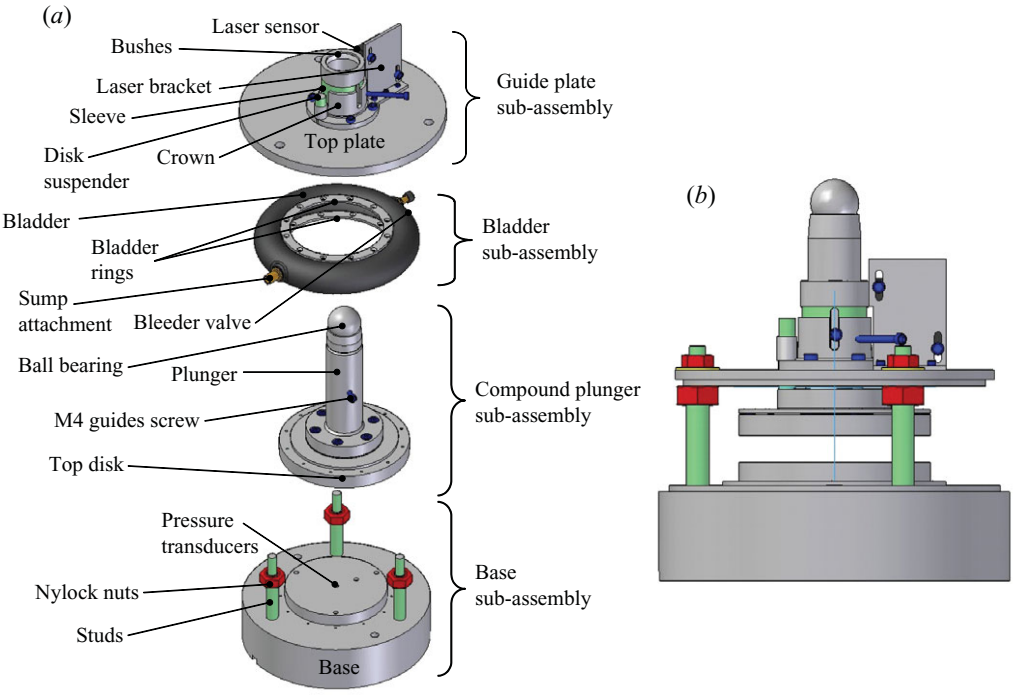


FIGURE 2. (Colour online) (*a*) Components of test cell. (*b*) Test cell assembly.

testing. Ambient pressure in the bladder was controlled using a simple header tank (not shown), and pressures were monitored at the centre of the lower disk through a PCB model M109B12 piezotronic transducer. A Keyence LB12 laser sensor was used to monitor the position of the upper disk. Glycerine ($\mu = 1.63$ N·s m^{-2} and $\rho = 1262$ kg m^{-3}) was used as the working fluid, the temperature of which was appropriately monitored.

Data for a typical case are considered, corresponding to an initial disk separation of about 10 mm and a mass of 30 kg falling through a height of 200 mm with a transmission efficiency (see § 1) of 70.7 %, resulting in about 41.6 J being dissipated in the fluid. The data of five identical tests were averaged. Thereafter, output voltages were converted into pressure (p_{meas}) and displacement (h) traces, the latter of which were smoothed to obtain velocity ($\dot{h}$) and acceleration ($\ddot{h}$) variations with time (t) of the upper disk. Figure 3 shows variations of p_{meas}, h, $\dot{h}$ and $\ddot{h}$ with t for a typical test, in which the thinner lines immediately adjacent to p_{meas} are uncertainty bounds.

3. Computational fluid dynamics predictions

We used the commercial computational fluid dynamics (CFD) software package Fluent to conduct computer experiments, with a domain defined by $R \geqslant r \geqslant 0$ and $h \geqslant z \geqslant 0$ (see figure 1) and the boundary conditions given by

$$v_r = v_z = 0 \quad \text{at} \quad z = 0; \quad v_r = 0, \; v_z = -\frac{\mathrm{d}h}{\mathrm{d}t} \quad \text{at} \quad z = h(t); \quad h(0) = h_0; \quad p(R) = 0. \tag{3.1}$$

https://doi.org/10.1017/S0022112010005756 Published online by Cambridge University Press

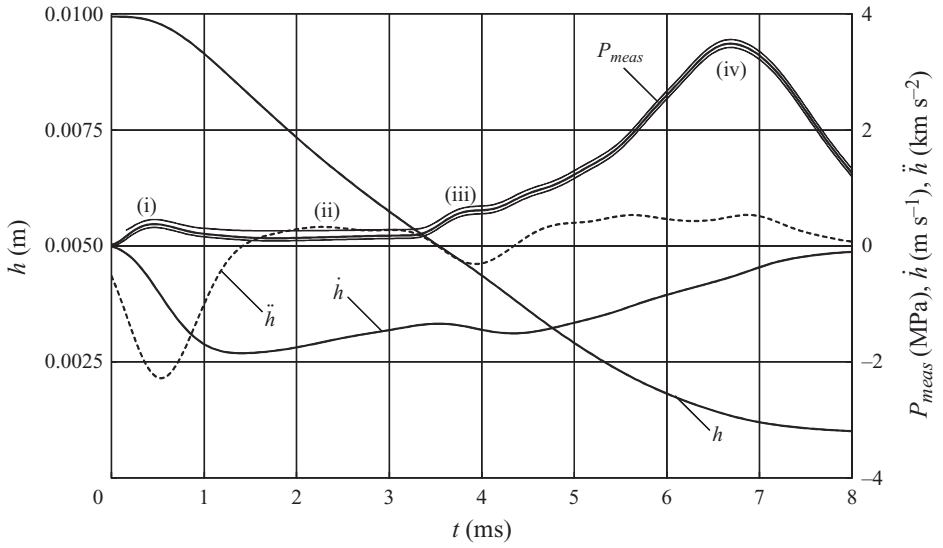


FIGURE 3. Measured variations of pressure at the centre of the lower disk (adjacent thinner lines are uncertainty bounds), disk separation, disk velocity and disk acceleration with time.

Fluent solves the equations of mass and momentum conservation formulated in terms of primitive variables – pressure, density and velocity. A pressure-implicit-with-splitting-of-operators pressure–velocity coupling scheme was used, part of the SIMPLE family of algorithms and recommended by Fluent for transient problems.

Inputs of $\dot{h} \equiv \mathrm{d}h/\mathrm{d}t$ were required for Fluent in analytical form. For this purpose polynomials of order 21 and 7 were fitted to the measured variations of $\dot{h}$ with t for $6\,\mathrm{ms} \geqslant t \geqslant 0\,\mathrm{ms}$ and $8\,\mathrm{ms} \geqslant t \geqslant 6\,\mathrm{ms}$ respectively. A grid of stationary cells of constant mesh size 0.1 mm in the radial and vertical directions was set up, which was used in conjunction with a time step of 1×10^{-5} s. The scheme operates in such a way that adjacent rows of cells are merged when the cell height adjacent to the upper moving boundary is less than or equal to 20 % of the nominal cell height of 0.1 mm. Mesh independence was inferred by establishing that small (less than 5.3 %) differences existed between predictions of pressures for this case and one having a mesh size of 0.05 mm with a time step of 0.5×10^{-5} s. The maximum difference in pressure between these cases was 0.025 MPa.

Figure 4 shows the measured $\dot{h}$ data and the polynomial fits to these data, together with CFD predictions (for the two different meshing schemes) of pressure variations at the centre of the lower disk.

4. Analysis

4.1. *Development of quasi-steady linear model*

The equations of motion pertinent to the system shown in figure 1 are as follows in the streamfunction–vorticity format, where the pressures generated are sufficiently low such that liquid bulk compressibility effects have been neglected:

$$\frac{\partial \omega}{\partial t} + r v_r \frac{\partial(\omega/r)}{\partial r} + v_z \frac{\partial \omega}{\partial z} = \nu \left[\frac{\partial}{\partial r} \frac{1}{r} \frac{\partial(\omega r)}{\partial r} + \frac{\partial^2 \omega}{\partial z^2} \right], \tag{4.1}$$

https://doi.org/10.1017/S0022112010005756 Published online by Cambridge University Press

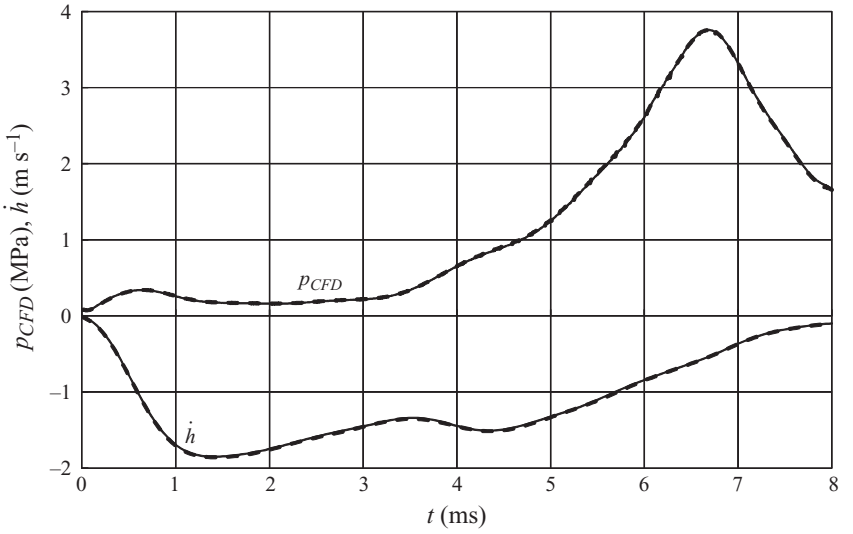


FIGURE 4. Measured variations of disk velocity ($\dot{h}$) with time shown as the solid line and polynomial fits to the data as the broken line; CFD predictions of pressure variations (p_{CFD}) with time at the centre of the lower disk, where the broken line represents data arising from a mesh size of 0.1 mm with a time step of 1×10^{-5} s, and the solid line represents data arising from a mesh size of 0.05 mm with a time step of 5×10^{-6} s.

where

$$\omega \equiv \frac{\partial v_z}{\partial r} - \frac{\partial v_r}{\partial z} = \frac{1}{r}\frac{\partial^2 \psi}{\partial z^2} + \frac{\partial}{\partial r}\frac{1}{r}\frac{\partial \psi}{\partial r}, \quad v_r = -\frac{1}{r}\frac{\partial \psi}{\partial z}, \quad v_z = \frac{1}{r}\frac{\partial \psi}{\partial r}, \tag{4.2}$$

and the boundary conditions are given by (3.1).

The formulation of Phan-Thien, Sugeng & Tanner (1987) uses the parallel assumption (see for example Engman *et al.* 2005) corresponding to the self-similarity of the velocity profiles defined by $v_z = \dot{h}g$ and $v_r = -[r\dot{h}/(2h)]g'$, where $1 \geqslant g(\eta, t) \geqslant 0$, $g' \equiv \partial g/\partial \eta$, $\eta \equiv z/h$ and $\dot{h} \equiv \mathrm{d}h/\mathrm{d}t$. The system is generally subject to $h_0/R \ll 1$ (Drazin & Riley 2006) and is described by

$$g'''' - \lambda g'' - \frac{h^2}{\nu}\frac{\partial}{\partial t}g'' - Re(g-\eta)g''' = 0, \tag{4.3}$$

where the dimensionless coefficients are defined as

$$Re \equiv \frac{h\dot{h}}{\nu} \quad \alpha \equiv \frac{\ddot{h}h}{\dot{h}^2} \quad \lambda \equiv Re(\alpha - 2) \equiv Re\Re. \tag{4.4}$$

The scaling has been chosen in such a way that the components $|g|$, $|g'|$, $|g''|$, $|g'''|$ and $|g''''|$ are of order unity. Thus, the dimensionless coefficient λ of the second term in (4.3) is approximately representative of the magnitude of that term. In considering the final term ($Re(g-\eta)g'''$) it is important to note that the purely inviscid case yields $g = \eta$, while subsequent derivations (see figure 5*a*) indicate variations of g with η that do not deviate much from linearity, suggesting that $|g - \eta| \leqslant O(0.1)$ for $0 \geqslant \lambda \geqslant -2\pi^2$. Hence the magnitude of the term is $\varepsilon|Re|$, where $\varepsilon \ll O(1)$.

Ab initio we consider situations in which both the third and final terms in (4.3) may be neglected, consistent with $|\lambda| \gg (h^2/\nu)|\partial g''/\partial t|$ and $|\lambda| \gg \varepsilon|Re|$ respectively,

https://doi.org/10.1017/S0022112010005756 Published online by Cambridge University Press

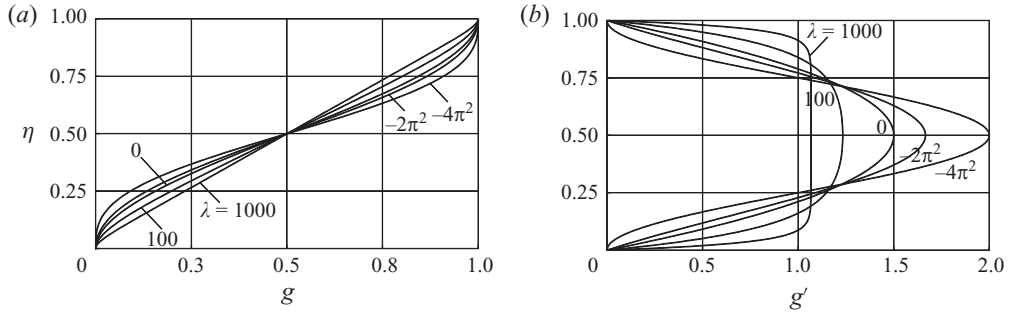


FIGURE 5. Variations of the dimensionless (*a*) axial and (*b*) radial velocities across the gap for various values of λ.

thus reducing (4.3) to

$$g'''' - \lambda g'' = 0 \tag{4.5}$$

and representing a quasi-steady linear (subsequently referred to as QSL) system in which the highest-order term g'''' has been retained. Discarding the third term in (4.3) is consistent with the assumption of a quasi-steady system for which the velocity profile shape changes with time are considered negligible relative to other effects. However, it must be clarified that the main temporal inertia effects are still embodied in the coefficient λ, which in fact represents the ratio of temporal inertia to viscous effects.

For this system, the dimensionless axial and radial velocities are respectively given by

$$g \equiv \overline{v}_z = \frac{(\cosh[\sqrt{\lambda}\eta] - 1) - (\sinh[\sqrt{\lambda}\eta] - \sqrt{\lambda}\eta)\coth[\sqrt{\lambda}/2]}{\sqrt{\lambda}\coth[\sqrt{\lambda}/2] - 2}, \tag{4.6}$$

$$g' \equiv \overline{v}_r = \frac{\sinh[\sqrt{\lambda}\eta] - (\cosh[\sqrt{\lambda}\eta] - 1)\coth[\sqrt{\lambda}/2]}{\coth([\sqrt{\lambda}/2] - 2/\sqrt{\lambda}} \tag{4.7}$$

with the pressure distribution

$$\frac{1}{r}\frac{\partial p_{QSL}}{\partial r} = \frac{\rho}{2}\left[\frac{\ddot{h}}{h}g' - \nu\frac{\dot{h}}{h^3}g'''\right] = \frac{\mu}{2}\frac{\dot{h}}{h^3}\left[\lambda g' - g'''\right], \tag{4.8}$$

which becomes

$$\frac{1}{r}\frac{\mathrm{d}p_{QSL}}{\mathrm{d}r} = \frac{\mu}{2}\frac{\dot{h}}{h^3}[\lambda g'_{\eta=0} - g'''_{\eta=0}] = \frac{\mu}{2}\frac{\dot{h}}{h^3}\left\{\frac{\coth[\sqrt{\lambda}/2]}{\coth[\sqrt{\lambda}/2] - 2/\sqrt{\lambda}}\right\} \tag{4.9}$$

on the lower disk. Comparisons between pressures at the centre of the lower disk predicted by (4.9) and numerical computations are shown in figure 6. These data are sufficiently close throughout the range such that (4.9) is regarded as an adequately representative model and is thus used for subsequent comparisons and calculations.

4.2. *Limiting cases of QSL model*

In order to further interrogate the physical mechanisms, we are also interested in two simple limiting cases of (4.5):

Case I

For $|Re| \to 0$ and $|\lambda| \equiv |h^2\ddot{h}/(\nu\dot{h}) - 2Re| \to \infty$, in the asymptotic limit of zero velocity but finite fluid acceleration, inviscid forces dominate; it is permissible to discard g'''',

https://doi.org/10.1017/S0022112010005756 Published online by Cambridge University Press

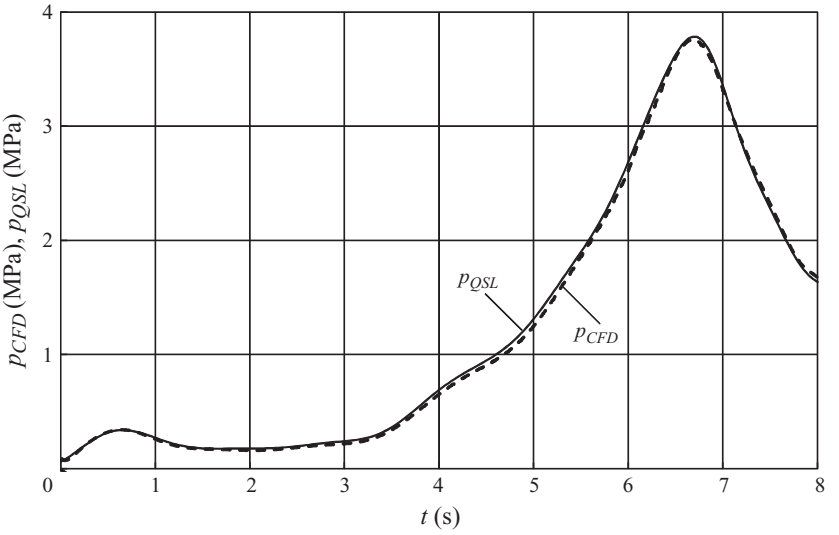


FIGURE 6. Pressures predicted by the CFD (with a mesh size of 0.05 mm and time step of 5×10^{-6} s) and QSL models at the centre of the lower disk.

and (4.3) adopts the following elementary form:

$$g'' = 0. \tag{4.10}$$

Solution of (4.10) yields the following dimensionless axial and radial velocities and pressure distribution:

$$g \equiv \overline{v}_z \equiv v_z/\dot{h} = \eta, \quad g' \equiv \overline{v}_r \equiv -\frac{2}{r}\frac{h}{\dot{h}}v_r = 1, \quad \frac{1}{r}\frac{\partial p_i}{\partial r} \equiv \frac{1}{r}\frac{\mathrm{d}p_i}{\mathrm{d}r} = \frac{1}{4}\mu\frac{\dot{h}}{h^3}Re(2\alpha - 3). \tag{4.11}$$

Case II

When $|\lambda| \ll 1$, the viscous system prevails and (4.3) becomes

$$g'''' = 0, \tag{4.12}$$

with the dimensionless axial and radial velocities and pressure distribution given by

$$g = \eta^2(2\eta - 3), \quad g' = -6(\eta^2 - \eta), \quad \frac{1}{r}\frac{\partial p_v}{\partial r} \equiv \frac{1}{r}\frac{\mathrm{d}p_v}{\mathrm{d}r} = 6\mu\frac{\dot{h}}{h^3}. \tag{4.13}$$

For the QSL system embodied in (4.5), figures 5(a) and 5(b) illustrate the dimensionless axial ($g \equiv v_z/\dot{h}$) and radial ($g' \equiv -2h/(r\dot{h})v_r$) velocity profiles respectively, for various values of the parameter λ, which represents the ratio of temporal inertia to viscous effects and may be conceptually regarded as a velocity profile shape parameter. It is noteworthy in the context of figure 5(b) that the wall shear stress generally increases with λ, with a corresponding thinning of the boundary layer. The limiting case $\lambda \to 0$ is synonymous with the purely parabolic viscous solution of case II, while $\lambda \to \infty$ gives the uniform variation of radial velocity in case I. As expected, figure 5(a) shows that the axial velocity profiles become increasingly linear with η as $\lambda \to \infty$.

4.3. *Basis of comparisons between experiment and analysis*

A basis was required for comparing measurements with predictions. For this purpose, measured variations of h, $\dot{h}$ and $\ddot{h}$ were substituted into (4.9), (4.11) and (4.13), thus providing predicted pressure variations with time for the three cases presented in §§ 4.1

https://doi.org/10.1017/S0022112010005756 Published online by Cambridge University Press

and 4.2, which could be reconciled with the pressure measurements. It is emphasized that this is no different in principle from implementing a specified value of $\dot{h} = \text{constant}$ into the well-documented constant velocity model for example, and then comparing the measured and predicted pressures to establish the validity of that model.

5. Results and discussion

The context of the current work was the flow evolution with time between two parallel disks and the corresponding pressure variations at the centre of the lower disk that occur subsequent to an impact-loading situation arising from dropping a mass from a fixed height onto the upper disk. As discussed in § 1, the situation does not correspond to one in which the top disk moves with a constant velocity; nor can it be interpreted as one for which the force on it is constant. Because the gravitational potential energy of which the major portion is ultimately dissipated in the fluid between the disks through the action of friction is specified, we refer to the system as a constant energy one. In this context, while the cases of constant velocity or constant force are fundamental, we propose that a system in which a constant amount of energy is to be dissipated through impact is equally fundamental. The current experimental data reflect typical features that were also identified during other tests that were conducted.

The current work is distinct from previous studies and concentrates on (i) clearly identifiable features that occur as a consequence of temporal inertia being dominant over spatial inertia, (ii) the asymptotic and simplified limiting analyses and their relationship with the corresponding experimental data and (iii) the effectiveness of the QSL model.

From the outset, the close correlation achieved between the QSL model and numerical computations (figure 6) suggests that the self-similarity assumptions made in its derivation, together with neglecting the third and fourth terms in (4.3), have analytical validity. However, it is appropriate to further qualify this latter issue.

For this purpose, firstly the term $(h^2/\nu)|\partial g''/\partial t|$ was approximated to $(h^2/\nu)|\partial g''_{av}/\partial t|$, where $g''_{av} = 2\int_0^{1/2} g''\,d\eta = 2g'_{1/2}$, and was evaluated using (4.7). Secondly, the value of the parameter $\varepsilon \sim O(|g - \eta|)$ was chosen as 0.1, conservative in the context of the fact that the discussion in § 4.1 indicated that $\varepsilon \leqslant O(0.1)$ for $\infty \geqslant \lambda \geqslant -2\pi^2$, while the approximate range encountered in our experiment was $8000 \geqslant \lambda \geqslant -1$, for which ε would be expected to have generally lower values.

It is clear from figure 7 that the conditions $|\lambda| \gg (h^2/\nu)|\partial g''/\partial t|$ and $\lambda| \gg \varepsilon|Re|$ are generally met, substantially explaining the close correlation obtained between CFD data and the pressure variations with time at the centre of the lower disk, obtained from (4.9) and shown in figure 6. Thus the QSL model may be used in reconciling experimental measurements with theoretical predictions.

In examining the experimental data, the immediately apparent features in figure 3 are as follows: (i) a distinct preliminary pressure spike at about 0.5 ms, corresponding to very large accelerations (exceeding $2\,\mathrm{km\,s^{-2}}$) in the negative direction; (ii) an intermediate region with somewhat reduced pressures; (iii) a further smaller pressure spike consistent with less extreme accelerations than in (i); and (iv) immediately thereafter, as h reduces further, a rapid increase of pressure in the form of a major pressure spike. The feature in (iii) is attributable to a second impact of the drop weight, preceded by a bounce arising from the initial elastic impact. While this might have been regarded as equipment-dependent, it is typical of what would be expected

https://doi.org/10.1017/S0022112010005756 Published online by Cambridge University Press

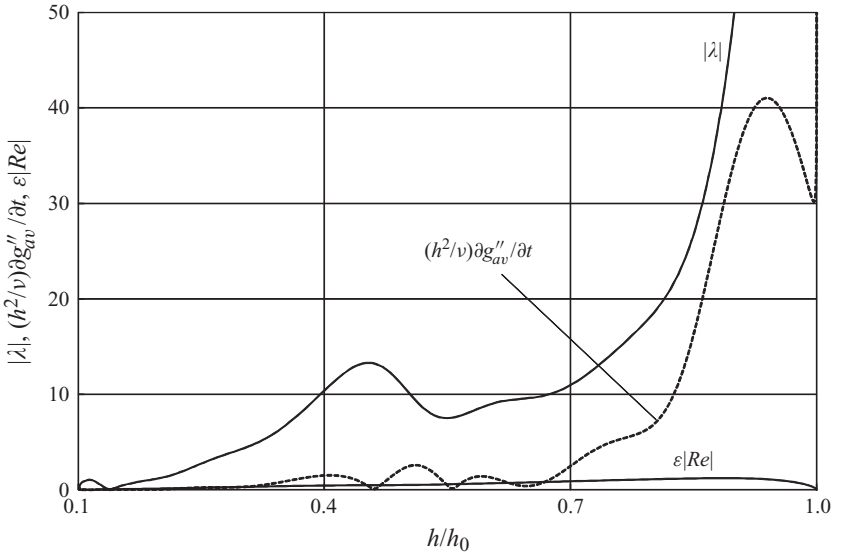


FIGURE 7. Variations of the parameters $|\lambda|$, $(h^2/\nu)\partial g''_{av}/\partial t$ and $\varepsilon|Re|$ with dimensionless disk separation (h/h_0).

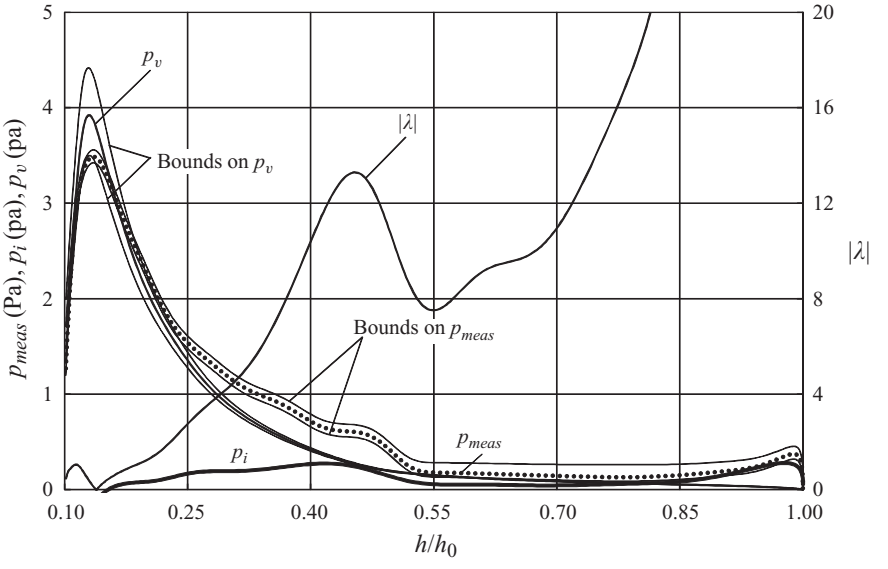


FIGURE 8. Variations of measured pressures at the centre of the lower disk (p_{meas}), and the asymptotic inviscid (p_i) and viscous (p_v) limiting cases, with dimensionless disk separation (h/h_0). Uncertainty bounds are given for p_{meas} and p_v. Shown on the same axes is the parameter $|\lambda|$ characterizing the ratio of temporal inertia to viscous effects.

in any facility of this type and, by virtue of the data processing strategy adopted (see §4.3), does not compromise the interpretation of data in any way.

Further processing of the data in figure 3 led to a comparison (figure 8) between measured pressures at the centre of the lower disk (p_{meas}) and the simple inviscid and viscous limiting solutions (p_i and p_v, arising from cases I and II respectively in §4.2), plotted against h/h_0. Superimposed on the same axes are variations of $|\lambda|$.

https://doi.org/10.1017/S0022112010005756 Published online by Cambridge University Press

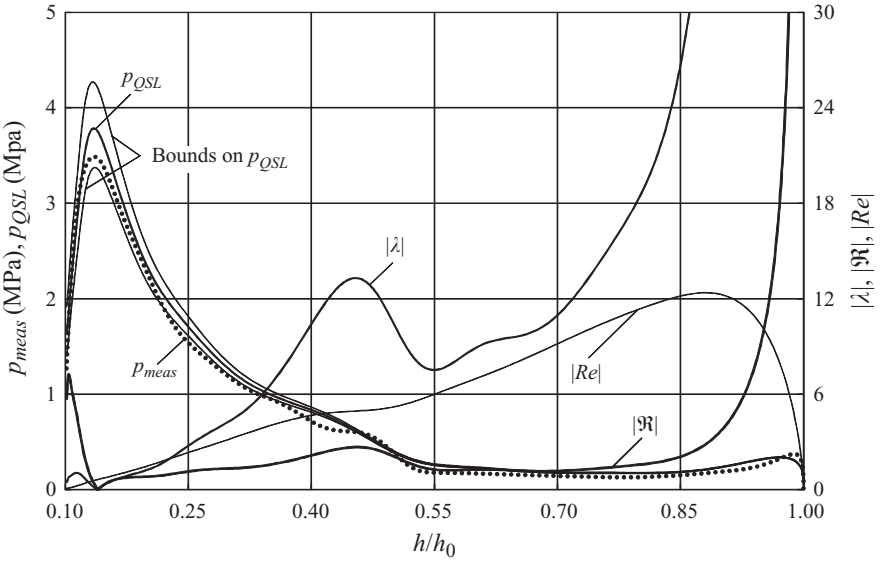


FIGURE 9. Variations of measured pressures at the centre of the lower disk (p_{meas}) and predictions (p_{QSL}) of the quasi-steady linear model, with dimensionless disk separation (h/h_0). Uncertainty bounds are given for p_{QSL}. Shown on the same axes are the parameter $|\lambda|$ characterizing the ratio of temporal inertia to viscous effects, the Reynolds number $|Re|$ and a parameter $|\Re|$ characterizing the ratio of temporal to spatial inertia terms.

Uncertainty bounds have been included for p_v and p_{meas} but are small for p_i and have been omitted for clarity. It is immediately clear that these limiting solutions reflect the broad features of the experimental data as $h/h_0 \to 0$ (large t) and $h/h_0 \to 1$ (small t) respectively. However, as would be expected, both solutions have diminishing legitimacy away from their respective asymptotes.

Figure 9 shows variations of p_{meas} and p_{QSL} with h/h_0, including uncertainty bounds for the latter. It is apparent that the QSL model closely follows the measurements throughout the range, including good correlation with the second-impact phenomenon (at $h/h_0 \sim 0.46$) mentioned previously, which was not achieved by either the viscous or the inviscid model.

Figures 10 and 11 include variations of p_{meas}, p_{QSL}, p_i and p_v in more detail for the smaller and larger values of h/h_0 respectively (uncertainty bounds have been omitted for clarity) – in addition to the parameters $|\lambda|$, $|\Re|$ and $|Re|$.

Interpretation of the data depends on an understanding of the interplay between temporal inertia, spatial inertia and viscous effects, as encapsulated in the simple relationship $|\lambda| = |Re||\Re|$, where $|\lambda|$, $|\Re|$ and $|Re|$ represent the approximate ratios of temporal inertia to viscous effects, temporal inertia to spatial inertia effects and spatial inertia to viscous effects, respectively.

In the limit $h/h_0 \to 1$ at the initial impact, $|Re| \to 0$ (see figures 9 and 11), from which the conclusion might have been drawn that viscous effects are dominant. However, this logic would be faulty, because both $|\lambda|$ and $|\Re|$ are very large in the same limit, with $|\lambda| \ll |\Re|$ (respective values of about 8000 and 212 000 were recorded). Therefore in this limit, temporal inertia dominates both spatial inertia and the effects of viscosity.

As h/h_0 diminishes with increasing time, $|\Re|$ drops off very sharply in the approximate range $1 > h/h_0 > 0.9$ and $|\lambda|$ less abruptly (figures 9 and 11). At

https://doi.org/10.1017/S0022112010005756 Published online by Cambridge University Press

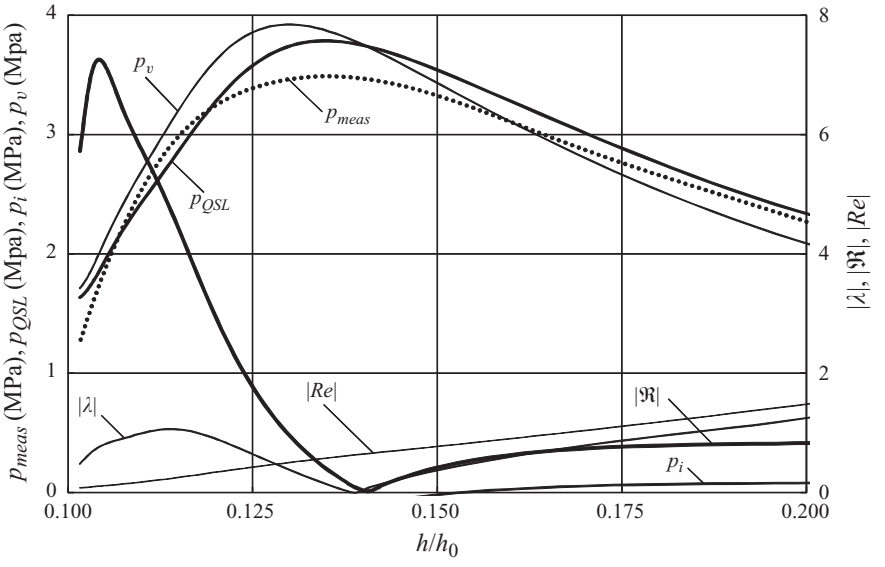


FIGURE 10. Same as figure 9 with the addition of p_i and p_v, emphasizing smaller values of h/h_0.

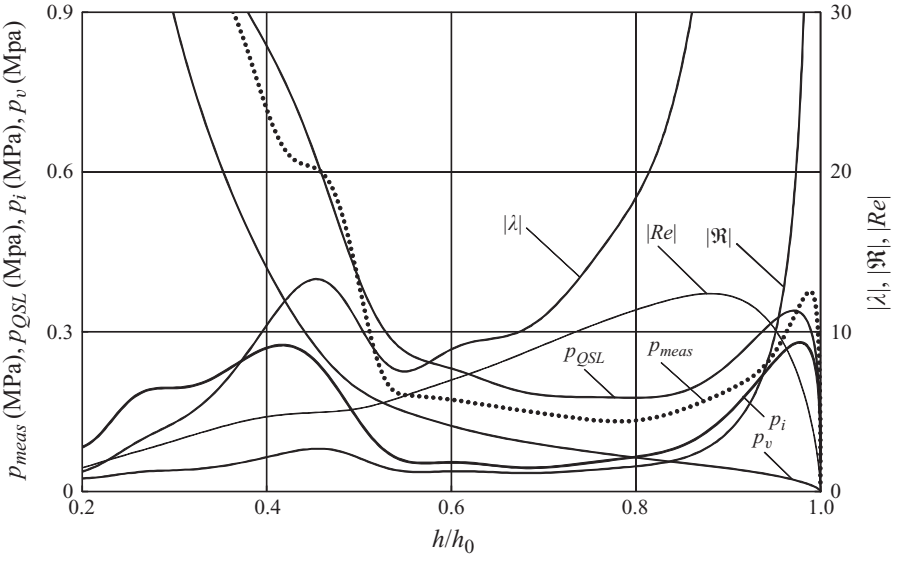


FIGURE 11. Same as figure 9 with the addition of p_i and p_v, clarifying the features occurring at larger values of h/h_0.

$h/h_0 \sim 0.999$, $|\Re|$ and $|\lambda|$ become equal in value (at about 710; not shown) corresponding to $Re = 1$, and beyond that point, $|\lambda| > |\Re|$, consistent with a progressive increase in Re towards a maximum value of about 12.39 and the fact that temporal inertia effects are becoming less dominant relative to spatial inertia effects, while both exceed the effects of viscosity. For $|\Re|$ the rate of decline becomes small at $h/h_0 \sim 0.7$, while $|\lambda|$ continues reducing, albeit at a moderate rate.

https://doi.org/10.1017/S0022112010005756 Published online by Cambridge University Press

In the approximate region $0.7 > h/h_0 > 0.55$, the term $\Re$ becomes $O(1)$, suggesting that spatial and temporal inertia effects are comparable in magnitude, while $|Re|$ and $|\lambda|$ are sufficiently large that viscosity is not yet important.

During the bounce phenomenon in (iii), corresponding to the approximate range $0.55 > h/h_0 > 0.35$ (peaking at $h/h_0 \sim 0.46$), both $|\lambda|$ and $|\Re|$ rise somewhat, to values of about 13.3 and 2.7 respectively, before diminishing once again. Here, temporal inertia is only somewhat larger than spatial inertia; however, it substantially exceeds the effects of viscosity.

Towards the end of the event, as h/h_0 declines further in the range $0.2 > h/h_0 > 0.1$ (see figures 9 and 10), both $|\lambda|$ and $|\Re|$ become progressively smaller, consistent with temporal inertia reducing relative to spatial inertia and $|Re|$ decreasing as viscous effects become more dominant. At $h/h_0 \sim 0.17$, $|\lambda|$ and $|\Re|$ become equal in magnitude (corresponding to $Re = 1$), and beyond that point, $|\Re| > |\lambda|$, for which $|Re| < 1$. In the region of $h/h_0 \sim 0.14$, both the parameters $|\lambda|$ and $|\Re|$ change sign and thereafter achieve peaks of $|\lambda| \sim 1$ and $|\Re| \sim 7.25$ at $h/h_0 \sim 0.115$ and 0.104 respectively, after which they decline. Even though temporal inertia effects considerably exceed those of spatial inertia near the peak, $|\lambda| < 1$ and $|Re| \ll 1$; hence viscous effects are now substantially larger than both temporal inertia and spatial inertia.

In summary, temporal inertia effects dominate relative to both spatial and viscous effects in the initial stages of the phenomenon, consistent with the characteristic pressure feature in (i) in figure 3, associated with very high accelerations of the upper disk and satisfactory comparisons with the inviscid model derived in § 4.2. Beyond that time, spatial and temporal inertia effects become of comparable magnitude in region (i), while viscous effects remain small. In (iii) the bounce phenomenon causes a further pressure increase similar to (i), but with a less pronounced dominance of temporal inertia over the other effects. After the pressure peak in (iii) viscous effects begin increasing, and a point is reached at which the Reynolds number is unity, beyond which the temporal inertia terms once again become progressively larger than those of spatial inertia. As the event progresses towards its end, viscous effects become increasingly dominant over other effects, consistent with diminishing Reynolds numbers and the major pressure rise in (iv). In this region, despite the fact that temporal inertia effects are substantially larger than spatial inertia, they are inconsequential relative to viscous effects. As might be expected, the simple viscous model correlates well with measured data in this limit.

6. Conclusions

(i) A unique impact experiment was conducted, whereby a mass was dropped from a fixed height onto a top disk, initially separated by a small distance from a lower axisymmetric stationary disk, with liquid (glycerine) between the disks. The highly dynamic squeeze-film system that evolved was experimentally determined by monitoring pressure variations with time at the centre of the lower disk, together with instantaneous disk separation.

The experiment corresponds neither to a classical constant velocity nor to a constant force situation. Because the largest part of the gravitational potential energy (dictated by the initial height of the mass above the upper disk) was dissipated in the fluid between the disks through the action of friction, we refer to this fundamental system as a constant energy one.

(ii) The equations of motion from a well-established self-similarity approach were reduced to a simpler (quasi-steady linear or QSL) form appropriate to the experiment,

https://doi.org/10.1017/S0022112010005756 Published online by Cambridge University Press

using order-of-magnitude arguments. Measured values of disk separation, velocity and acceleration were substituted as inputs into three analytical models (for which closed-form solutions exist): the full QSL model and two limiting cases, namely an inviscid and a viscous model. On the basis of pressures at the centre of the lower disk, the QSL model provided excellent comparisons, both with measurements and with data generated by a commercial CFD software package, throughout the duration of a typical experiment, while the inviscid and viscous models achieved good correlations during the initial impact and towards the end of the experiment, respectively.

(iii) The parameters used to characterize the system were as follows: $|\Re|$, the ratio of temporal to spatial inertia effects; $|\lambda|$, the ratio of temporal inertia to viscous effects; and $|Re|$, the ratio of spatial inertia to viscous effects.

(iv) Four main features were identified: (*a*) a preliminary pressure spike associated with the initial impact, corresponding to a dominance of temporal inertia effects over both spatial inertia and viscous effects; (*b*) an intermediate region having lower pressures, with temporal and spatial inertia effects of comparable magnitude (and both substantially exceeding viscous effects); (*c*) a repeat-impact (bounce) phenomenon in which temporal inertia once again dominates, but to a lesser extent than in (*a*); and (*d*) the final region in which viscous effects become significantly larger than both spatial and temporal inertia.

(v) Region (*a*) exhibits an important new phenomenon, previously not reported on, that is likely to typify effects that would be commonly observed in impact systems involving squeeze-film flows.

REFERENCES

Berman, A. S. 1953 *J. Appl. Phys.* **24**, 1232.

Brady, J. F. 1984 *Phys. Fluids* **27**, 1061.

Brady, J. F. & Acrivos, A. 1981 *J. Fluid Mech.* **112**, 127.

Brindley, G., Davies, J. M. & Walters, K. 1976 *J. Non-Newton. Fluid Mech.* **1**, 19.

Drazin, P. G. & Riley, N. 2006 *The Navier–Stokes Equations: A Classification of Flows and Exact Solutions.* Cambridge University Press.

Engmann, J., Servais, C. & Burbidge, A. S. 2005 *J. Non-Newton. Fluid Mech.* **132**, 1.

Espin, L. & Papageorgiou, D. T. 2009 *Phys. Fluids* **21**, 113601.

Hamza, E. A. & MacDonald, D. A. 1981 *J. Fluid Mech.* **109**, 147.

Ishizawa, I. 1966 *Japan Soc. Mech. Engng* **9** (35), 533.

Jones, A. F. & Wilson, S. D. R. 1975 *ASME J. Lubr. Technol.* **97**, 101.

Kuzma, D. C. 1967 *Appl. Sci. Res.* **18**, 15.

Kuzma, D. C., Maki, E. R. & Donnelly, R. J. 1964 *J. Fluid Mech.* **19**, 395.

Lawrence, C. J., Kuang, Y. & Weinbaum, S. 1985 *J. Fluid Mech.* **156**, 479.

Oseen, C. W. 1927 *Neuere Methoden und Ergebnisse in der Hydrodynamik Leipzig.* Akademische Verlagsgesellschaft.

Phan-Thien, N., Dudek, J., Boger, D. V. & Tirtaatmadja, V. 1985 *J. Non-Newton. Fluid Mech.* **18**, 227.

Phan-Thien, N., Sugeng, F. & Tanner, R. I. 1987 *J. Non-Newton. Fluid Mech.* **24**, 97.

Rashidi, M. M., Shahmohamadi, H. & Dinarvand, S. 2008 *Math. Probl. Engng* **2008**, 935095.

Reynolds, O. 1886 *Phil. Trans. R. Soc. Lond.* **177**, 157.

Stefan, J. 1874 *Kais. Akad. Wiss. Math. Nat. Wien* **69** (2), 713.

Stuart, J. T., DiPrima, R. C., Eagles, P. & Davey, A. 1990 *Math. Phys. Sci.* **430** (1879), 347.

Tichy, J. A. 1981 *Appl. Sci. Res.* **37** (3–4), 301.

Tichy, J. A. & Modest, M. F. 1978 *ASME J. Lubr. Technol.* **100** (3), 316.

Tichy, J. A. & Winer, W. O. 1970 *ASME J. Lubr. Technol.* **92**, 588.

Wang, C. Y. 1976 *ASME J. Appl. Mech.* **98**, 579.

Weinbaum, S., Lawrence, C. J. & Kuang, Y. 1985 *J. Fluid Mech.* **156**, 463.

https://doi.org/10.1017/S0022112010005756 Published online by Cambridge University Press